Experimental Characterization of Frequency-Dependent Series Resistance and Inductance for Ground Shielded On-Chip Interconnects

Diego M. Cortés-Hernández, Reydezel Torres-Torres, *Member, IEEE*, Oscar González-Díaz, and Mónico Linares-Aranda, *Member, IEEE*

***Abstract*—This paper presents an exhaustive analysis of the frequency-dependent series resistance and inductance associated with the distributed model of on-chip interconnects including a ground shield to reduce substrate losses. This analysis identifies the regions where the resistance and inductance curves present different trending due to variations in the current distribution. Furthermore, the apparent discrepancy of experimental curves with the well-known square-root-of-frequency models for the resistance and inductance considering the skin-effect is explained. Measurement results up to 40 GHz show that models involving terms proportional to the square root of frequency are valid provided that the section of the interconnect where the current is flowing is appropriately represented.**

***Index Terms*—IC interconnects, ground shield, skin effect.**

I. Introduction

As technology evolves, integrated circuits (ICs) increase the metal layers used for interconnection purposes [1]. Many of these interconnects are routed in a very complex way and are operated at microwave frequencies, which causes considerable signal attenuation and delay. Thus, to avoid the inherent losses attributed to the substrate, a ground shield is included between the signal traces and the semiconductor substrate, which introduces even more complexity when analyzing the frequency dependent behavior of these interconnects [2]. Nonetheless, from an IC design point of view, developing efficient and broadband models is necessary. For this purpose, interconnects can be treated as transmission lines (TLs) formed at different levels of the circuit, and thus presenting different electrical characteristics.

Traditionally, IC designers were particularly concerned about the series resistance (R) and shunt capacitance (C) presented by a TL, as well as for the number of lumped-circuit stages required to represent a line of certain length within a given bandwidth [3], [4]. This motivated research oriented to determine and represent these parameters as a function of geometry, frequency (f), and fabrication materials [5]–[9]. For C, several models were developed showing a weak dependence on f and negligible losses, represented by means of a shunt conductance (G), when the interconnect presents a ground shield [10]–[14]. In contrast R, which is associated with the metal losses occurring along the interconnect, is strongly dependent on f and it is expected to be proportional to the square root of f when the skin depth is comparable or less than the thickness of the metal layer [15], [16]. Nevertheless, this ideal trending of R is not evident in the vast majority of the experimental results obtained for on-chip interconnects [11], [17], [18] even when separately analyzing the attenuation constant associated with the metal losses [1], [17], [19]. For this reason, several research groups explained the apparent deviation of the R versus f curves from the square-root-of-f models by analyzing the variation of the current flow distribution with f [6], [16], [20]. Nevertheless, many of these models use fitting parameters to compensate for effects that are still not well explained. For instance, assuming that the resistance that the interconnect presents at low frequencies introduces an f-independent parameter that is observed even at very high frequencies [8], [15].

On the other hand, as f increases, the RC model used in many design stages lacks accuracy, especially for relatively long interconnects such as those used for global networks (e.g., clock distribution) [21]. In this case, including the series inductance (L) is mandatory and thus the corresponding variation with f has to be understood to develop reliable models. Here, a characterization of the series R and L impacted by f-dependent effects is presented. In this analysis, both parameters exhibit five frequency regions associated with proximity and skin effects related to the geometry of the ground plane and the conductive strip.

II. Theory

For planar TLs, once the operation frequency is so high that the metal skin depth (δ) is smaller than the thickness of the metal layers used to form the signal trace and ground plane (t and t_g, respectively), R and L become dependent on f. Particularly, for TLs guiding signals in quasi-TEM mode, when $\delta \ll t$, it

Manuscript received May 11, 2013; revised February 19, 2014; accepted December 3, 2013. Date of publication June 10, 2014; date of current version December 11, 2014. This work was supported in part by CONACyT-Mexico under Grants 261691 and 154337.

D. M. Cortés-Hernández, R. Torres-Torres, and M. Linares-Aranda are with the Department of Electronics, Instituto Nacional de Astrofísica, Óptica y Electrónica (INAOE), Tonantzintla, Puebla 72840, Mexico (e-mail: dmcortes@inaoep.mx).

O. González-Díaz is with the Intel Guadalajara Design Center, Tlaquepaque, Jalisco 45700, Mexico.

Color versions of one or more of the figures in this paper are available online at http://ieeexplore.ieee.org

Digital Object Identifier 10.1109/TEMC.2014.2321580

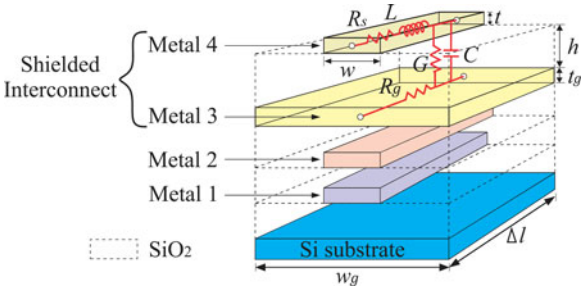

Fig. 1. Stack-up for IC interconnects. In this particular example, the Metal-3 level is used as the reference plane and the Metal-4 contains the signal strip.

is expected that R is proportional to $\sqrt{f}$, whereas L decreases as predicted by a term that is inversely proportional to $\sqrt{f}$ [15]. Although this behavior is clearly observed in packaging technologies at microwave frequencies, it is not evident for IC interconnects. This is due to the fact that the dimensions of the layers forming the latter are much smaller than in packaging technologies, which originates that the effect of R and L is more accentuated. Furthermore, this makes the corresponding variation with f more noticeable, allowing to observe the skin and proximity effects in the signal and ground plane within different f-ranges.

Fig. 1 shows a typical stack-up defining the different metal layer levels within an IC. In this figure, the ground plane is located at the Metal-3 level. This plane is commonly formed by a grid that can be considered as a solid metal layer since the corresponding pattern presents dimensions much smaller than the wavelength of microwave signals. The ground plane presents a width w_g and shields the upper interconnects from the substrate to reduce the losses associated with eddy currents and undesired coupling. In this figure, h is the thickness of the SiO_2 layer separating the ground plane from the signal trace, which presents a width w.

Fig. 1 includes an interconnect with length $l = \Delta l$ that can be represented by means of lumped per-unit-length *RLGC* elements. Although these elements have been widely studied in the literature, the dependence of R and L on f is simplified most of the times assuming a $\sqrt{f}$ variation with a constant proportionality coefficient. Further examination of this assumption is the subject of study in this paper. Thus, in order to graphically support the explanations presented in this section, Fig. 2 shows results from full-wave simulations of an interconnect, where the current distributions within the signal and ground plane are illustrated at different f.

A. Resistance

In accordance to Fig. 1, the total series resistance of the interconnect can be defined as

$$R = R_s + R_g \tag{1}$$

where R_s is the resistance associated with the signal trace, whereas R_g corresponds to the ground plane. Owing to the fact that these two resistive contributions to R are located at different regions of the structure, the configuration of the electromagnetic

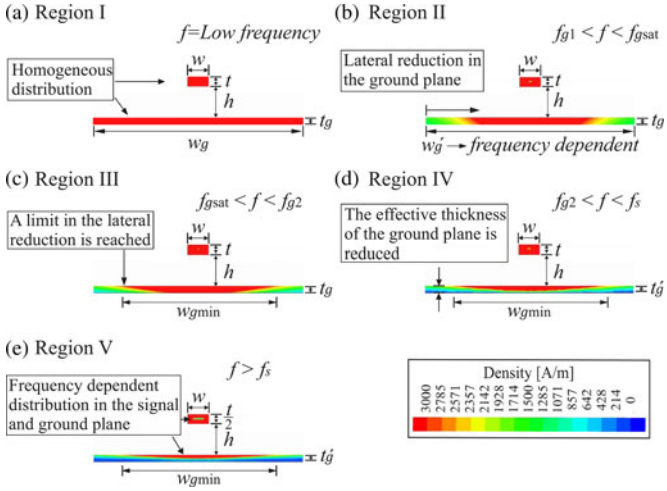

Fig. 2. Current density distributions within an interconnect at different frequencies obtained through full-wave simulations of a line presenting: $w = 2\ \mu$m, $t = 925$ nm, $h = 3\ \mu$m, $t_g = 640$ nm, and $w_g = 20\ \mu$m.

fields will affect the distribution of the current flow in a different way as f changes.

Starting the analysis at f so low that δ is much bigger than t and t_g, both R_s and R_g can be analyzed assuming DC conditions. For the case of R_s, since the current can be considered to uniformly flow within the cross section of the signal trace, the following equation can be used:

$$R_s = R_{s0} = \frac{1}{\sigma w t} \tag{2}$$

where σ (given in S/m) is the conductivity of the metal. For R_g, the corresponding value in a conventional design is usually negligible (i.e., $R_{g0} \approx 0$) [22]. However, although the magnitude of R_g at low frequencies is small, it can be approximately calculated as [5], [6]:

$$R_g = R_{g0} = \frac{1}{\sigma w_g t_g} \tag{3}$$

where w_g is the total width of the ground plane as shown in Fig. 2(a). Thus, in accordance to (1)–(3), when plotting the experimentally obtained R versus f curve, the starting point at $f \approx 0$ is $R = R_{s0} + R_{g0}$, which remains constant within the f-range labeled as region I in the conceptual plot shown in Fig. 3. The series resistance in this region can thus be defined as follows:

$$R_{\mathrm{I}} = R_{s0} + R_{g0}. \tag{4}$$

In Fig. 3, R remains constant until f reaches a value (i.e., f_{g1}) that makes the resistance to proportionally increase with $\sqrt{f}$. This first transitional frequency is associated with the reduction of the effective width (w_g') of the cross section where the current is flowing within the ground plane as f increases; this implies that for $f > f_{g1}$, w_g is substituted by w_g' in (3), which is explained as follows. At low f, the transverse fields surrounding the signal trace reach the top of the ground plane near below it and also laterally penetrate the whole plane since δ is very big, which allows to calculate R_g from (3). Thus, when f increases to

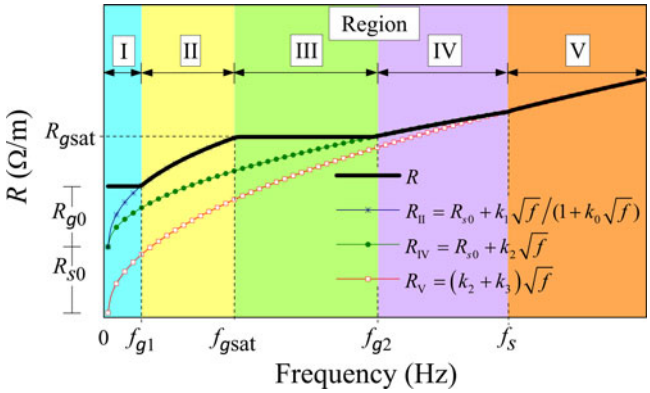

Fig. 3. Conceptual plot showing the regions presenting different variation of the *R* versus *f* curve.

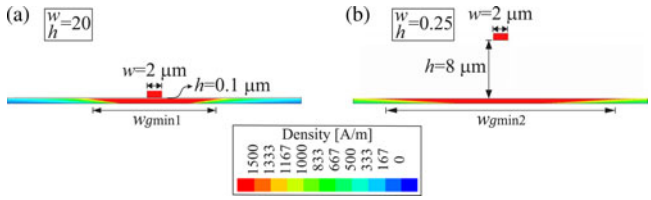

Fig. 4. Simulations showing the impact of the *w*/*h* ratio on the minimum width of the section where the current is flowing within the ground plane.

a value at which δ becomes comparable to the total width of the ground plane, the TL operates in region II, where w_g' decreases with δ, which is illustrated in Fig. 2(b). Notice in Fig. 3, that in this region *R* is expected to increase with $\sqrt{f}$ until w_g' reaches a minimum width ($w_{g\,\min}$) that corresponds to the area below the signal strip where the electric field considerably penetrates the ground plane from the top. In other words, the width of the section where the current is flowing in the ground no longer suffers side reduction beyond $w_{g\,\min}$; this occurs at $f = f_{g\mathrm{sat}}$. Consequently, the effective width of the ground plane in region II is the sum of $w_{g\,\min}$ plus the side penetration of the current at each side of the plane, which is approximately given by 2δ provided that $w_g' > w_{g\,\min}$. Hence, considering that within this *f*-region δ is bigger than the dimensions of the signal trace (which is a reasonable assumption in most practical technologies), R_s in (1) remains constant, and *R* presents a dependence on *f* attributed to R_g and described by (3) assuming $w_g' = w_{g\,\min} + 2\delta$. Thus, *R* in region II can be approximately expressed as follows:

$$R_{\mathrm{II}} = R_{s0} + \frac{k_1\sqrt{f}}{1 + k_0\sqrt{f}} \tag{5}$$

where $k_1 = 1/2d\sigma t_g$, $k_0 = w_{g\,\min}/2d$ and d is a constant related to δ. Here, it is important to remark the fact that $w_{g\,\min}$ depends on the dimensions of the structure, particularly, on the separation between the signal trace and the ground plane. In Fig. 4, full-wave simulations were used to illustrate an increase in this parameter as *h* increases. Alternatively, an empirical way to obtain an approximate value for $w_{g\,\min}$ is explained in [22].

Once $f = f_{g\mathrm{sat}}$, it is expected that *R* remains constant since R_g no longer suffers reduction once $w_g' = w_{g\,\min}$ as shown in Fig. 2(c). This is true as long as the effective thickness the ground plane is not impacted by the skin effect (i.e., $t_g \ll \delta$). Within this *f*-range, defined as region III and also illustrated in Fig. 3, *R* can approximately be represented by

$$R_{\mathrm{III}} = R_{s0} + R_{g\mathrm{sat}} \tag{6}$$

where $R_{g\mathrm{sat}} \approx 1/\sigma w_{g\,\min} t_g$.

When $\delta > t_g$, a reduction in the effective thickness of the ground plane is observed as *f* increases. This originates a confinement of the current concentration on top of the ground plane [see Fig. 2(d)], proportionally increasing R_g with $\sqrt{f}$. This occurs in region IV illustrated in Fig. 3, where *R* can be represented by

$$R_{\mathrm{IV}} = R_{s0} + k_2\sqrt{f} \tag{7}$$

where k_2 is a proportionality constant related to the skin effect in the transversal section of the ground plane. Notice that in region IV, due to the configuration of the fields, once the cross-sectional area for which the current is flowing is reduced as *f* increases, most of the current is confined to the upper section of the ground plane. Conversely, for the signal trace, the current is confined in comparable proportions along the perimeter of its cross section [see Fig. 2(e)]. In fact, this is the reason why when considering that the signal and ground plane present the same thickness, the vertical skin effect is observed in the ground plane at lower frequencies. Approximately, R_s starts to become *f*-dependent at $f = f_s$ (i.e., when $\delta \approx t/2$), which defines the onset frequency for region V. Thus, the corresponding expression for obtaining *R* in this region is

$$R_V = k_2\sqrt{f} + k_3\sqrt{f} = k_4\sqrt{f} \tag{8}$$

where k_3 is a proportionality constant related to the skin effect in the signal strip and $k_4 = k_2 + k_3$. Notice that (8) is the typical expression expected for a variation of *R* with *f*. From our analysis, we observe that this expression is only valid once all the cross sections for which the current is flowing through a homogeneous line become frequency dependent.

B. Inductance

Regarding the total inductance (*L*) of a planar and homogeneous TL, this is composed by two terms called internal L_{int} and external L_{ext} inductances, which are associated with the current loop formed along its length by the signal and ground paths [22]. Mathematically, the total inductance can be calculated from

$$L = L_{\mathrm{int}} + L_{\mathrm{ext}}. \tag{9}$$

In Fig. 5, L_{ext} and L_{int} are associated with the area of the parts of the current loop outside and inside the metals, respectively. In accordance to Fig. 5, L_{int} varies with *f* when the current distribution changes in the signal trace and ground plane due to the current crowding and skin effects. Since this variation is different in these two metal regions, L_{int} can be represented by means of the sum of the inductance associated with the signal trace (L_s), and that of the ground plane (L_g).

Notice that the sketch in Fig. 5 showing a perspective a section of TL oversimplifies the analysis of the inductance. This is due

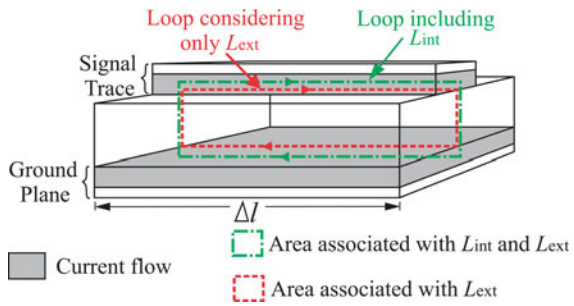

Fig. 5. Side view of a TL identifying the parts of the current loop defining the internal and external inductances.

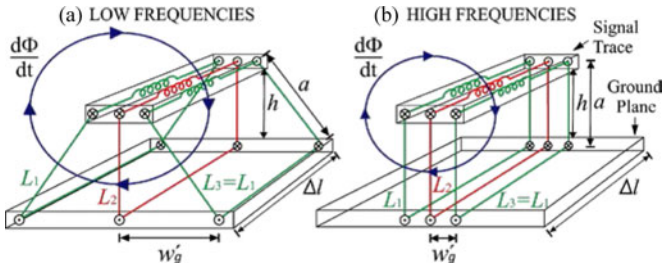

Fig. 6. Illustration of the reduction in the outer components of the inductance loop when *f* increases: (a) low frequencies, and (b) high frequencies.

to the fact that it suggests that the current flowing along the TL always forms loops that are perpendicular to the signal trace and ground plane. To show that this is not always the case, the following analysis is presented.

Assume that *L* is divided along the width of the TL in three inductances that are connected in parallel L_1, L_2, and L_3, as illustrated in Fig. 6(a) (notice that $L_1 = L_3$ for a symmetrical TL). Each one of these inductances is thus associated with a loop that presents different form depending mainly on the distribution of the current in the ground plane. Therefore, at low frequencies, the outer inductance components (i.e., L_1 and L_3) are originated by a loop with larger area than corresponding to L_2 since the current in the signal trace is farther from the ground plane. As *f* increases, however, the current in the ground plane is confined near below the signal trace and reduces the area of the loops associated with L_1 and L_3, which in turns reduces the total inductance [see Fig. 6(b)]. The effect described in this paragraph is responsible of additional dependence of *L* on *f* that is observed in practical on-chip interconnects.

Similarly as in the case for *R*, different variations on *L* are observed in the five *f*-regions previously discussed where the current distribution changes with *f*. Thus, when the TL operates in region I, the current is homogeneously distributed within the signal trace and ground plane yielding a maximum value for the internal inductance since the current loop covers from the top of the signal trace to the bottom of the ground plane, whereas the loops associated with L_1 and L_3 present a maximum area. In this case, L_s and L_g present constant values L_{s0} and L_{g0}, respectively. Thus, total inductance in this *f*-region is independent of *f* and can be written as

$$L_{\mathrm{I}} = L_{s0} + L_{g0} + L_{\mathrm{ext0}} = L_0. \tag{10}$$

The term L_{ext0} represents the external inductance that can be obtained at low frequencies from the dimensions of the line [6]. When *f* increases and reaches f_{g1}, the TL operates in region II. In this case, the effective width (w'_g) where the current is flowing in the ground plane decreases laterally due to the current crowding and skin effects. These effects reduce the area formed by the current loops associated with L_1 and L_3, which change L_{ext} and L_{int}. This is an important observation since in classic literature it is assumed that the external inductance is always independent of frequency [15].

In order to analyze the inductance in region II, the effective inductances L_1, L_2, and L_3, which are assumed to represent the three different zones defining the inductance of the TL as shown in Fig. 6 are considered. For this case, L_1 and L_3 are proportional to the distance *a* defined in Fig. 6, which is calculated as

$$a = \sqrt{h^2 + w_g'^2} = h\sqrt{1 + \frac{k_\delta}{f}} \tag{11}$$

where k_δ is a proportionality constant that depends on the properties of the materials and on the geometry of the TL since w_g' was assumed to be inversely proportional to $\sqrt{f}$ (due to its variation with δ). Thus, to obtain a general expression for the inductance in region II, we assume that L_1 and L_3 are effective inductances considering all the current loops formed at the outer side of the TL. Since these inductances are proportional to *a*, using (11) it is possible to write

$$L_1 = L_3 = L_{\mathrm{x1}}\sqrt{1 + \frac{k_\delta}{f}} \approx L_{\mathrm{x1}} + \frac{L_{\mathrm{x2}}}{f} \tag{12}$$

where L_{x1} is the value at which L_1 and L_2 tend when the current in the ground plane is confined just below the signal trace as in Fig. 6(b), $L_{x2} = k_\delta/2$, and an expansion in Taylor series was used to obtain a linear equation since $k_\delta/f \ll 1$ can be assumed. Notice that (12) is valid only in region II.

Now, considering the combined effect of L_1, L_2, and L_3, which are in parallel connection, L_{II} can be calculated by

$$L_{\mathrm{II}} = \frac{1}{\frac{1}{L_1} + \frac{1}{L_2} + \frac{1}{L_3}} = \frac{p + nf}{1 + mf} \tag{13}$$

where L_2 is assumed to be constant (see Fig. 6), $m = (2L_2 + L_{\mathrm{x1}})/L_{\mathrm{x2}}$, $n = L_2 L_{\mathrm{x1}}/L_{\mathrm{x2}}$ and $p = L_2$. Notice that L_{II} was expressed as in (13) to provide a simplified expression that allows to obtain the total inductance in region II as a function of *f*. Alternatively, L_{II} can be written in terms of the external and internal inductances; however, in this particular region, the parallel connection of the three inductances makes difficult to distinguish the contribution of the internal and external inductances to *L*.

Once *f* rises up to a value so high that the interconnect is operating in region III, the external inductance presents its minimum value (L_∞) which remains constant from this frequency range on. Furthermore, the internal inductance remains at an approximately constant value ($L_{\mathrm{int}} = L_{s1} + L_{g1}$). This is due to the

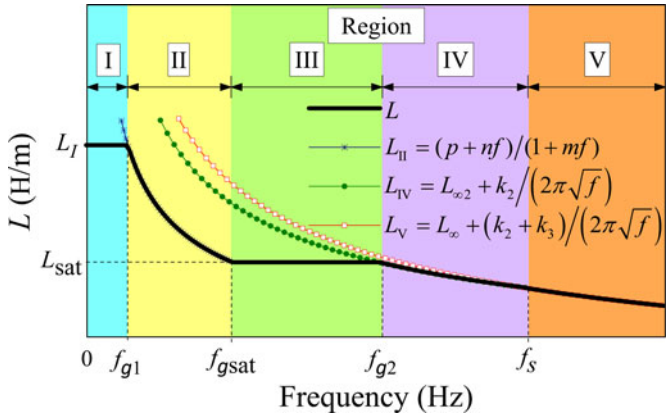

Fig. 7. Conceptual plot showing the regions presenting different variation of the L versus f curve.

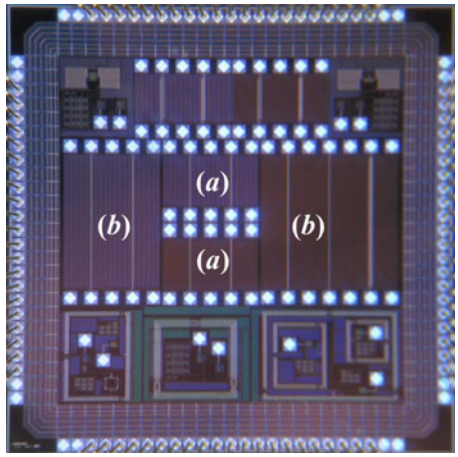

Fig. 8. Photograph of fabricated microstrip lines that have lines of (a) 400 μm and (b) 1000 μm. Other test structures have not label in the photograph.

fact that the current distribution in the metals presents no significant modification provided that the skin depth is larger than the thickness of the signal trace and ground plane. Therefore, in region III, the inductance can be represented as a constant function of given by

$$L_{\rm III} = L_{s1} + L_{g1} + L = L_{\rm sat} \tag{14}$$

where L can be calculated considering the area of the current loop formed between the signal trace and ground plane at high frequencies, whereas $L_{\rm sat}$ is the total inductance presented at the smallest frequency at which the current distribution can be associated with the conceptual sketch in Fig. 6(b).

As f continues increasing, the skin effect becomes apparent again, vertically reducing the area from which the current is flowing in the ground plane, which occurs in region IV. On the other hand, the internal inductance in the signal trace remains without change since the current distribution in this trace presents no variation in region IV. The reason for this is argued earlier when discussing the variation of R in this region. Thus, the expression for region IV is

$$L_{\rm IV} = L_{s1} + \frac{k_2}{2\pi\sqrt{f}} + L_\infty = L_{\infty 2} + \frac{k_2}{2\pi\sqrt{f}} \tag{15}$$

where $L_{\infty 2} = L_{s1} + L_\infty$, and k_2 is the constant defined in (7).

Finally, at frequencies where the skin effect impacts the current distribution in the signal trace (i.e., region V), the internal inductance associated with both the signal and ground conductors varies with f. In this case, the typical expression used for modeling the inductance of planar TLs can be used [15]. This is

$$L_{\rm V} = \frac{k_2}{2\pi\sqrt{f}} + \frac{k_3}{2\pi\sqrt{f}} + L_\infty = L_\infty + \frac{k_4}{2\pi\sqrt{f}} \tag{16}$$

which is analogous to (8). Fig. 7 shows a frequency spectrum illustrating the variation of inductance within the different operation regions.

III. Prototypes and Measurements

A test vehicle was designed and fabricated to verify the validity of the analysis presented in this paper. In this regard, several microstrip lines with different lengths, widths, and heights from the ground plane were included so that it is possible to systematically identify aforementioned regions.

The simplified representation shown in Fig. 1 corresponds to the stack-up for the employed fabrication process. The microstrip lines were made of aluminum in the Metal-1 level and present widths of 2 and 4 μm, and lengths of 400 and 1000 μm. One set of these lines presents a ground shield at the Metal-1 level, whereas another set presents this shield at the Metal-3 level. Thus, the thickness of the SiO_2 dielectric for these lines is $h = 3$ μm for the first set, and $h = 1$ μm for the second one. In all cases, the signal trace presents a nominal thickness $t = 925$ nm, whereas the metal thickness of the ground shields is $t_g = 665$ nm and $t_g = 640$ nm when implemented in the Metal-1 ($h = 3$ μm) and Metal-3 ($h = 1$ μm), respectively. Fig. 8 shows a photograph of the fabricated lines.

The microstrip lines are terminated with ground–signal–ground pads so that RF-coplanar probes presenting a pitch of 150 μm can be used to perform S-parameter measurements. The measurements were performed in a frequency span ranging from 0.01 to 40 GHz using a vector network analyzer which was previously calibrated up to the probe tips by applying a line-reflect-match algorithm and an impedance-standard-substrate provided by the probe manufacturer. Afterward, the propagation constant γ and characteristic impedance Z_c were determined from the experimental data of each pair of microstrip lines, presenting identical cross section and varying only in length. For this purpose, a line–line procedure was applied to remove the parasitic effects associated with the pads [23]. Thus, once the γ and Z_c are obtained from measured data, the experimental series resistance and inductance versus frequency curves are, respectively, determined as $R = Re(\gamma \cdot Z_c)$ and $L = Im(\gamma \cdot Z_c)/2\pi f$. This allows the direct inspection of these parameters to identify the different operation regions.

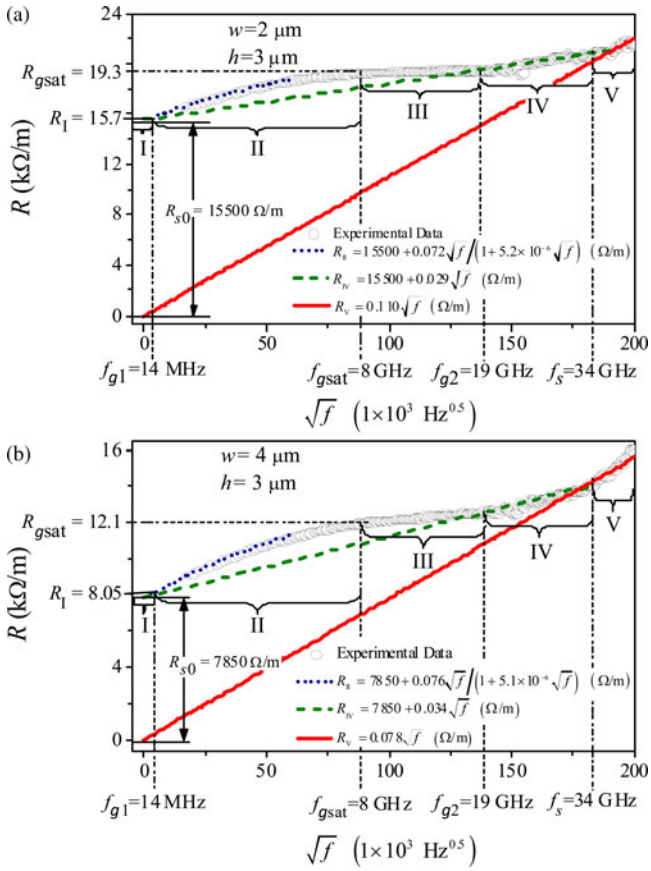

Fig. 9. Experimental R versus $\sqrt{f}$ curves up to $f = 40$ GHz for the microstrip lines presenting the ground plane in Metal-1 level: (a) $w = 2$ μm, and (b) $w = 4$ μm.

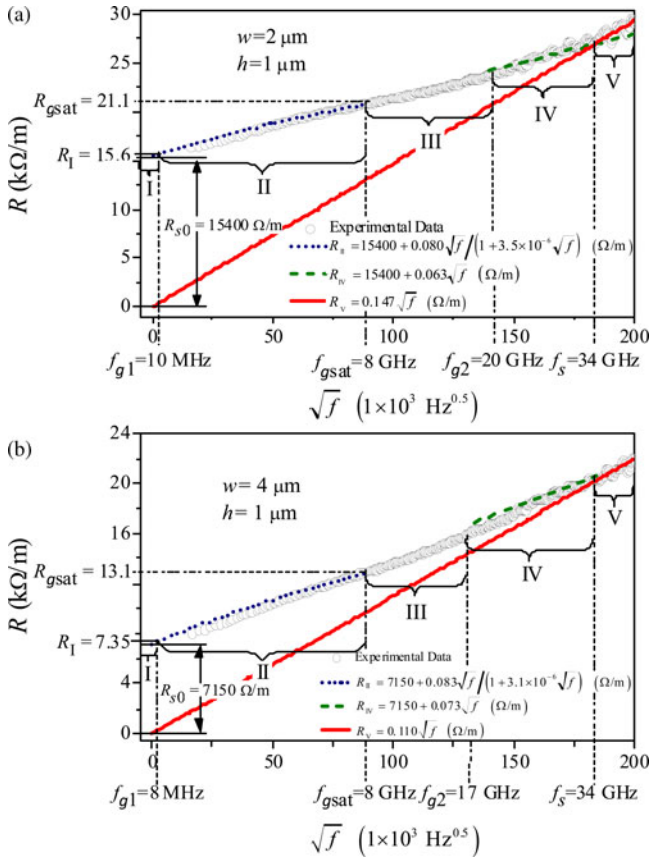

Fig. 10. Experimental R versus $\sqrt{f}$ curves up to $f = 40$ GHz for the microstrip lines presenting the ground plane in Metal-3 level: (a) $w = 2$ μm, and (b) $w = 4$ μm.

IV. Experimental Results and Discussion

Since R approximately linearly increases with $\sqrt{f}$ when the current crowding and skin effects become apparent, it is convenient to plot the experimental R versus $\sqrt{f}$ curve to identify the previously analyzed regions. Fig. 9(a) and (b) shows these data for microstrip lines presenting different widths for the signal trace and the ground plane in Metal-1 level ($h = 3$ μm). Since the cross section of the metals forming these lines define R at very low frequencies where region I takes place, the widest line in Fig. 9 presents a smaller value for $R_I = R_{s0} + R_{g0}$ obtained. It is important to remark the fact the sum of R_{s0} and R_{g0} was obtained from extrapolation of experimental data since direct determination of $R = Re(\gamma Z_c)$ at very low frequencies is difficult. The consistency that the obtained values for these parameters show for the different lines, however, verifies the validity of the extrapolations. As f increases, region II can be observed in the plots of Fig. 9 by noticing a linear increase of R with $\sqrt{f}$. This region is observed in both lines within the same frequency range. Moreover, k_1 and k_0 take approximately the same value to represent $R_{\rm II}$ for both lines, which means that the lateral skin effect occurring in the ground plane increases R roughly in the same proportion independently of the line width. This behavior continues up until region III becomes apparent. In this case, a plateau is observed in the R versus $\sqrt{f}$ curves, meaning that the lateral skin effect in the ground plane reached saturation since the current is confined below the signal trace. This region remains until the skin depth equals the thickness of the ground plane, where the resistance increases again proportionally with $\sqrt{f}$ in region IV. Notice that, similarly as k_1 and k_0 in region II, k_2 in both lines in Fig. 9 presents approximately the same value. Besides, another interesting observation is that in regions I, II, III, and IV, R_s remains constant (i.e., $R_s = R_{s0}$) since the skin depth is not comparable with the thickness of the signal trace. Thus, R_s becomes frequency dependent until the skin depth is smaller than one half of the signal trace thickness as explained in Section II. This occurs in region V, where R is represented by a line that passes through the origin since R_s and R_g are frequency dependent and there is no justification to add a constant to the model of R. R_V is typically the model used to represent the frequency-dependent resistance of TLs. Nonetheless, this model is only valid for on-chip interconnects at considerably high frequencies.

Fig. 10 shows the R versus $\sqrt{f}$ curves corresponding to two additional lines presenting the same widths considered in Fig. 9 but now including the ground plane closer to the signal trace this is the $h = 1$ μm case (i.e., at the Metal-3 level). As expected, at low frequencies, these lines present similar resistance

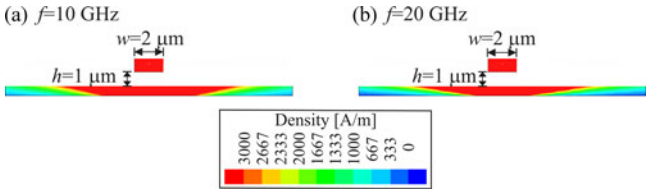

Fig. 11. Simulations pointing out the change in current distribution at the bottom of the ground plane within region III.

TABLE I
TRANSITION FREQUENCIES OBTAINED FOR THE FABRICATED LINES

Structure	f_{g1} (MHz)	f_{gsat} (GHz)	f_{g2} (GHz)	f_s (GHz)
$w = 2\ \mu$m, $h = 3\ \mu$m	14.2	8	19	34
$w = 4\ \mu$m, $h = 3\mu$m	13.7	8	19	34
$w = 2\ \mu$m, $h = 1\ \mu$m	9.8	8	20	34
$w = 4\ \mu$m, $h = 1\ \mu$m	8.2	8	17	34

$R_{\rm I}$ that their counterparts in Fig. 9. However, since the fields associated with the propagating signal are more confined in this second case, the forces experienced transversally by the current become stronger. This makes that small variations in the fields impact in a more accentuated way the distribution of the current. Notice, for instance, that the plateau that is expected to occur in region III is barely observed in the data shown in Fig. 10, which suggests an overlap between the different operation regions of the TLs. This is explained using the full-wave simulation results presented in Fig. 11. When the current distribution in the ground plane reaches saturation [see Fig. 11(a)], it is expected that the transversal section of ground plane presents no change with *f*. In fact, at frequencies beyond $f_{g\rm sat}$ but smaller than f_{g2}, the inductance is expected to remain constant. However, notice in Fig. 11(b) that even though no significant change in the effective width of the ground plane is observed on top, the bottom part presents a significant change, which explains the variation of *L* with *f* within this region.

Table I summarizes the experimentally obtained transition frequencies obtained for the fabricated lines. It is interesting to observe that $f_{g\rm sat}$ remains practically constant for all the measured structures. This is because $w_{g\,\rm min}$ is almost the same for all these cases, which implies that the effective width of the ground plane reaches saturation at approximately the same frequency for all these structures. Thus, even though the geometry is different for the four structures, the corresponding *w*/*h* ratio is not sufficiently different as to significantly modify the value of $w_{g\,\rm min}$.

The following transition frequency is related to the vertically skin effect in the ground plane (f_{g2}), to determine the frequency value at which this effect occurs, we observe the transition graphically in Fig. 9. Finally, the skin effect in the conductor strip (f_s) occurs when the skin effect reaches half the thickness of the strip, so the thickness for the strip is identified through the transition at higher frequencies. The transition frequencies values are presented in Table I.

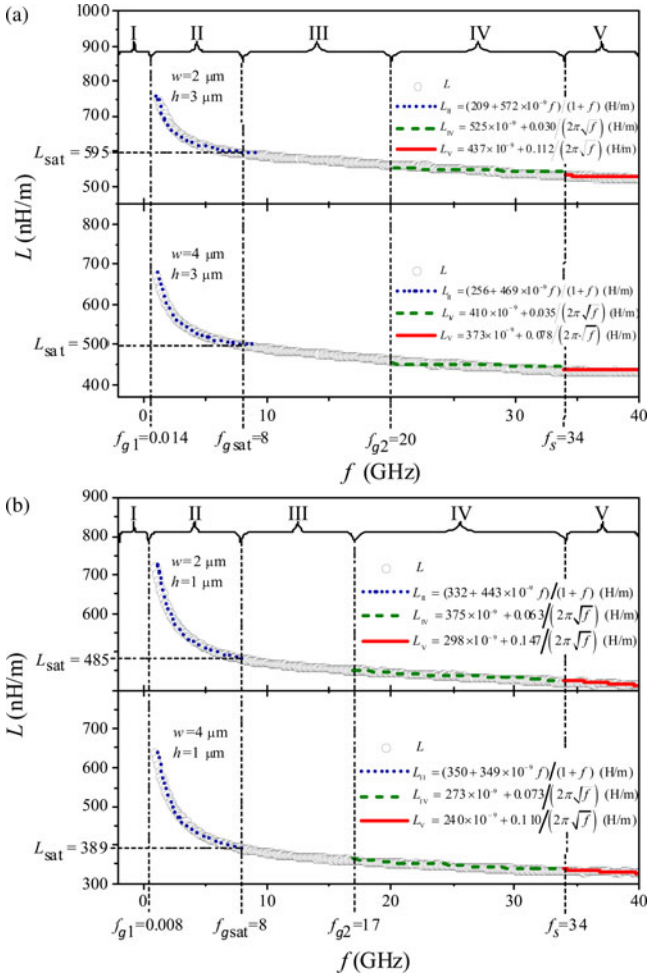

Fig. 12. Experimental *L* versus $\sqrt{f}$ curves for the fabricated lines presenting the ground plane at: (a) Metal-1 level, and (b) Metal-3 level.

When determining the parameters to represent *R* in the different operation regions, k_1, k_2, and k_4 are the coefficients that allow the representation of the corresponding frequency dependence within different frequency ranges. Thus, as discussed in Section II, for the case of *L* these parameters are the same since the skin effect impacts the series inductance and resistance in the same proportion. Thus, when using these coefficients together with the other parameters included in equations (13)–(16) (e.g., determined through simple linear regressions of experimental data), it is possible to represent with accuracy the inductance in a consistent way. Fig. 12 shows the corresponding model-experiment correlation up to 40 GHz for all the fabricated lines. In this case, the operation regions are not as easily identified as in the case of the series resistance since the external inductance, which presents a relatively weak frequency dependence, presents a higher value than the internal inductance at frequencies of gigahertz. Nevertheless, even in this case, the extractions obtained for the case of *R* allow an adequate representation of the experimental inductance. Table II summarizes the different parameters obtained for *R* and *L*.

TABLE II
PARAMETERS OBTAINED TO REPRESENT R AND L

Ground Plane→		Level Metal-1 $h = 3\ \mu$m		Level Metal-3 $h = 1\ \mu$m	
Trace width→		2 μm	4 μm	2 μm	4 μm
RESISTANCE	R_{s0} ($k\Omega \cdot m^{-1}$)	15.50	7.85	15.40	7.15
	R_{g0} ($k\Omega \cdot m^{-1}$)	0.20	0.20	0.20	0.20
	R_{gsat} ($k\Omega \cdot m^{-1}$)	19.3	12.10	21.10	13.10
	k_0 ($\mu Hz^{-1/2}$)	5.2	5.1	3.5	3.1
	k_1 ($\Omega \cdot m^{-1} \cdot Hz^{-1/2}$)	0.072	0.076	0.080	0.083
	k_2 ($\Omega \cdot m^{-1} \cdot Hz^{-1/2}$)	0.029	0.034	0.063	0.073
	k_4 ($\Omega \cdot m^{-1} \cdot Hz^{-1/2}$)	0.110	0.078	0.147	0.110
INDUCTANCE	L_{sat} ($nH \cdot m^{-1}$)	595	500	485	389
	$L\infty 2$ ($nH \cdot m^{-1}$)	525	410	375	273
	$L\infty$ ($nH \cdot m^{-1}$)	437	373	298	240
	p	209	256	332	350
	n ($\times 10^{-9}$)	572	469	443	349

V. CONCLUSION

An exhaustive analysis for identifying the different operation regions affecting the frequency dependence of the series resistance and inductance of on-chip interconnects was carried out. From this analysis, it was possible to associate physical phenomena with the different variations occurring in these parameters at frequencies of gigahertz. Moreover, the separate models for the different regions allow the representation of experimental resistance and inductance data in an accurate and consistent way. This analysis then allows the implementation of physical models for the accurate representation of the series parasitics occurring in interconnects used in both analog and digital ICs.

REFERENCES

[1] T. Quémerais, *et al.*, "65-, 45-, and 32-nm aluminium and copper transmission-line model at millimeter-wave frequencies," *IEEE Trans. Microw. Theory Tech.*, vol. 58, no. 9, pp. 2426–2433. Sep. 2010.

[2] J. Fan, X. Ye, *et al.*, "Signal integrity design for high-speed digital circuits: Progress and directions," *IEEE Trans. Electromagn. Compat.*, vol. 52, no. 2, pp. 392–400, May 2010.

[3] T. Sakurai, "Approximation of wiring delay in MOSFET LSI," *IEEE J. Solid-State Circuits*, vol. SSC-18, no. 4, pp. 418–426, Aug. 1983.

[4] Y. I. Ismail, *et al.*, "Figures of merit to characterize the importance of on-chip inductance," *IEEE Trans. Very Large Scale Integr. Syst.*, vol. 7, no. 4, pp. 442–449, Dec. 1999.

[5] F. Schnieder, "Model of thin-film microstrip line for circuit design," *IEEE Trans. Microw. Theory Tech.*, vol. 49, no. 1, pp. 104–110, Jan. 2001.

[6] A. R. Djordjevic and T. K. Sarkar, "Closed form formulas for frequency dependent resistance and inductance per unit length of microstrip and strip transmission lines," *IEEE Trans. Microw. Theory Tech.*, vol. 42, no. 2, pp. 241–248, Feb. 1994.

[7] J. H. Kim, D. Oh, and W. Kim, "Accurate characterization of broadband multiconductor transmission lines for high-speed digital systems," *IEEE Trans. Adv. Packag.*, vol. 33, no. 4, pp. 857–867, Nov. 2010.

[8] J. Brinkhoff, K. S. S. Koh, K. Kang, and F. Lin, "Scalable transmission line and inductor models for CMOS millimeter-wave design," *IEEE Trans. Microw. Theory Tech.*, vol. 56, no. 12, pp. 2954–2962, Dec. 2008.

[9] T. Makita, *et al.*, "Coplanar waveguides on high-resistivity silicon substrates with attenuation constant lower than 1 dB/mm for microwave and millimeter-wave bands," *IEEE Trans. Electron Devices*, vol. 58, no. 3, pp. 709–715, Mar. 2011.

[10] D.F. Williams, "Metal-insulator-semiconductor transmission lines," *IEEE Microw. Theory Tech.*, vol. MTT-47, no. 2, pp. 176–181, Feb. 1999.

[11] H. Heng-Ming, *et al.*, "Millimeter-wave transmission line in 90-nm CMOS technology," *IEEE J. Emerging Sel. Topics Circuits Syst.*, vol. 2, no. 2, pp. 194–199, Jun. 2012.

[12] J. Zheng, Y.-C. Hahm, V. K. Tripathi, and A. Weisshaar, "CAD-oriented equivalent-circuit modeling of on-chip interconnects on lossy silicon substrate," *IEEE Trans. Microw. Theory Tech.*, vol. 48, no. 9, pp. 1443–1451, Sep. 2000.

[13] B. J. Rubin and H. L. Bertoni, "Waves guided by conductive strips above a periodically perforated ground plane," *IEEE Trans. Microw. Theory Tech.*, vol. MTT-31, no. 7, pp. 541–549, Jul. 1983.

[14] D. Zeng, H. Wang, *et al.*, "A novel equivalent circuit for on chip transmission lines modeling," in *Proc. Custom Integr. Circuits Conf.*, Sep. 2010, pp. 1–4.

[15] J. Zhang, et al. "Causal RLGC(f) models for transmission lines from measured S-parameters," *IEEE Trans. Electromagn. Compat.*, vol. 52, no. 1, pp. 189–198, Feb. 2010.

[16] J. C. Rautio and V. Demir, "Microstrip conductor loss models for electromagnetic analysis," *IEEE Trans. Microw. Theory Tech.*, vol. 51, no. 3, pp. 915–921, Mar. 2003.

[17] L. F. Tiemeijer, R. M. T. Pijper, R. J. Havens, and O. Hubert, "Low-loss patterned ground shield interconnect transmission lines in advanced IC processes," *IEEE Trans. Microw. Theory Tech.*, vol. 55, no. 3, pp. 561–570, Mar. 2007.

[18] H.-Y. Cho, J.-K. Huang, C.-K. Kuo, S. Liu, and C.-Y. Wu, "A novel transmission line deembedding technique for RF device characterization," *IEEE Trans. Electron Devices*, vol. 56, no. 12, pp. 3160–3167, Dec. 2009.

[19] M. Kärkkäinen, *et al.*, "Transmission line and lange coupler implementations in CMOS," in *Proc. Eur. Microw. Integr. Circuits Conf.*, Sep. 2010, pp. 357–360.

[20] G. E. Ponchak, A. Margomenos, and L. P. B. Katehi, "Low-loss CPW on low-resistivity Si substrates with a micromachined polyimide interface layer for RFIC interconnects," *IEEE Trans. Microw. Theory Tech.*, vol. 49, no. 5, pp. 866–870, May 2001.

[21] O. Gonzalez-Díaz, *et al.*, "A design-oriented methodology for accurate modeling of on-chip interconnects," *Analog Integr. Circuits Signal Process.*, vol. 71, pp. 221–230, May 2012.

[22] S. H. Hall, *et al.*, *Advanced Signal Integrity for High-Speed Digital Designs* vol. 1. New York, NY, USA: Wiley-IEEE Press, 2009.

[23] A. M. Mangan, *et al.*, "De-embedding transmission line measurements for accurate modeling of IC designs," *IEEE Trans. Electron Devices*, vol. 53, no. 2, pp. 235–241, Feb. 2006.

Diego M. Cortés-Hernández was born in Quindío, Colombia. He received the B.S. degree in electronics from the Universidad del Quindío, Quindío, in 2008, and the M.S. degree in electronics from the National Institute for Astrophysics, Optics and Electronics, Puebla, Mexico, in 2013, where he is currently working toward the Ph.D. degree by carrying out experimental analysis of interconnects operating at microwave frequencies. His areas of expertise include high-frequency measurement and characterization of devices as well as electromagnetic modeling of passive structures.

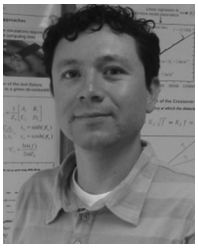

Reydezel Torres-Torres (S'01–M'06) received the Ph.D. degree from the National Institute for Astrophysics, Optics and Electronics (INAOE), Puebla, Mexico.

He was with Intel Laboratories in Mexico and IMEC in Belgium. He is currently a Senior Researcher in the Microwave Research Group of INAOE. He has authored more than 60 journal and conference papers and directed 5 Ph.D. and 15 M.S. theses, all in high-frequency characterization and modeling of materials, interconnects, and devices for microwave applications.

Oscar González-Díaz was born in Puebla, Mexico. He received the B.S. degree in electronics engineering from the Instituto Tecnológico de Puebla, Puebla, in 2004, and the M.S. and Ph.D. degrees in electronics from the National Institute for Astrophysics, Optics and Electronics, Puebla, in 2006 and 2011, respectively.

He is currently with Intel Laboratories, Mexico.

Mónico Linares-Aranda (M'01) received the M.Sc. degree in electronics from the National Institute for Astrophysics, Optics and Electronics (INAOE), Puebla, Mexico, and the Ph.D. degree in electrical engineering from the Center for Research and Advanced Studies of the National Polytechnic Institute, Ciudad de México, Mexico, in 1986 and 1996, respectively.

He joined the INAOE, in 1986, where is currently a Researcher in the Microelectronics Department. He has published more than 60 papers in international conferences and journals in the field of very large scale integration design and microelectromechanical systems (MEMS). His research interests include design, fabrication, and testing of mixed mode CMOS integrated circuits and MEMS.